amide gel electrophoresis (PAGE) (14% gel) along with bovine calmodulin as a standard for the estimation of the retinal calmodulin concentration on a Coomassie blue stained gel. *Drosophila* calmodulin was identified in the gel on the basis of the characteristic change in mobility in the presence of EGTA (~20 kD) or $Ca^{2+}$ (17 kD) [C. B. Klee, T. H. Crouch, M. H. Krinks, *Proc. Natl. Acad. Sci. U.S.A.* **76**, 6270 (1979)]. In addition, the calmodulin was the only major 20-kD retinal protein. Assuming all the retinal calmodulin was in the photoreceptor cells and that >80% of this calmodulin was in the rhabdomeres, we estimated the concentration of calmodulin per rhabdomere at 0.5 pg. Using previously determined measurements of the length and diameter of the *Drosophila* rhabdomere from R. C. Hardie [in *Progress in Sensory Physiology 5*, H. Autrum *et al.*, Eds. (Springer-Verlag, New York, 1983), p. 1] and assuming that 50% of the rhabdomeric volume was cytoplasmic, we estimated that the cytoplasmic volume of a rhabdomere was 0.05 pl and that the concentration of calmodulin in a rhabdomere was 0.5 mmol.

16. J. A. Porter and C. Montell, unpublished material.
17. F. Steele and J. E. O'Tousa, *Neuron* **4**, 883 (1990); F. R. Steele, T. Washburn, R. Rieger, J. E. O'Tousa, *Cell* **69**, 669 (1992).
18. A. D. Blest, in *Advances in Insect Physiology*, P. D. Evans and V. B. Wigglesworth, Eds. (Academic Press, London, 1988), p. 1.
19. The NINAC expression library was constructed by the generation of random size–selected DNA fragments (0.3 to 0.8 kb) from the cDNA, pc-*ninaC*-15 (*11*), encoding the full-length p174 as described by C. Montell, K. Jones, C. Zuker, and G. Rubin [*J. Neurosci.* **7**, 1558 (1987)] and subcloned into the Eco RI site of λgt11 [R. Young and R. Davis, *Proc. Natl. Acad. Sci. U.S.A.* **80**, 1194 (1983); R. A. Young and R. W. Davis, *Science* **222**, 778 (1983)]. The NINAC fragment library was screened with $^{125}$I-calmodulin (NEN, Boston) by the method of Phillips and co-workers (*7*), and 19 positives were plague-purified. The *ninaC* DNA inserted between the λ arms was amplified by asymmetric PCR, and the sequences of the ends of each clone were determined by dideoxy sequencing [P. C. McCabe, in *PCR Protocols: A Guide to Methods and Applications*, M. A. Innis, D. H. Gelfand, J. J. Sninsky, T. J. White, Eds. (Academic Press, San Diego, 1990), p. 76]. The 19 NINAC p174 calmodulin binding fragments extended from the following amino acids: 955 to 1130, 996 to 1128, 1009 to 1146, 1012 to 1145, 1029 to 1141, 1032 to 1195, 1035 to 1193, 1038 to 1282, 1043 to 1182, 1045 to 1222, 1048 to 1211, 1051 to 1191, 1058 to 1197, 1062 to 1201, 1065 to 1198, 1067 to 1226, 1079 to 1219, 1085 to 1252, and 1087 to 1253.
20. J. A. Porter and C. Montell, *J. Cell Biol.* **122**, 601 (1993).
21. The NINAC proteins expressed in P[*ninaC*$^{KD}$] and P[*ninaC*$^{MD}$] were missing amino acids 17 to 284 and 331 to 1032, respectively. The p174 derivative expressed in P[*ninaC*$^{\Delta B}$] was deleted for amino acids 1037 to 1253. The mutation in P[*ninaC*$^{\Delta B}$] prevents the synthesis of p132. The sizes of the truncated forms of p174 expressed in P[*ninaC*$^{KD}$], P[*ninaC*$^{MD}$], and P[*ninaC*$^{\Delta B}$] are 143, 93, and 145 kD, respectively. The transformants P[*ninaC*$^{KD}$] and P[*ninaC*$^{MD}$] were generated previously (*20*), and the *ninaC* mutation introduced into P[*ninaC*$^{\Delta B}$] was generated by oligonucleotide-directed mutagenesis according to methods described in (*13*). Briefly, single-stranded DNA was generated from a BluescriptKS+ (Stratagene) construct containing a 2.9 kb Kpn I *ninaC* genomic fragment (9.0 to 11.9 map units) (*13*). This DNA was used to create a new Pst I site, by oligonucleotide-directed mutagenesis, at nucleotide 3902 to 3907 in the unique sequence encoding p174. The new Pst I site and the existing Pst I site at 3249 were used to delete the coding sequence from amino acids 1037 to 1253. This deleted version of the *ninaC* gene was subcloned into the *P*-element transformation vector pDM30 and introduced into *ninaC*$^{P235}$ and *ry*$^{506}$ flies by *P*-element–mediated germline transformation [G. M. Rubin and A. C. Spradling, *Science* **218**, 348 (1982); A. C. Spradling and G. M. Rubin, *ibid.*, p. 341; D. Mismer and G. M. Rubin, *Genetics* **116**, 565 (1987)].
22. H. Swanljung-Collins and J. H. Collins, *J. Biol. Chem.* **267**, 3445 (1992).
23. E. Buchner, *J. Neurogenet.* **7**, 153 (1991).
24. B. T. Bloomquist *et al.*, *Cell* **54**, 723 (1988).
25. Z. Xia *et al.*, *Neuron* **6**, 431 (1991); Z. Xia *et al.*, *J. Neurochem.* **60**, 305 (1993).
26. C. W. Heizmann and K. Braun, *Trends Neurosci.* **15**, 259 (1992).
27. K. A. Alexander, B. M. Cimler, K. E. Meier, D. R. Storm, *J. Biol. Chem.* **262**, 6108 (1987); Y. Liu and D. R. Storm, *Trends Pharmacol.* **11**, 107 (1990).
28. J. R. Glenney Jr., A. Bretscher, K. Weber, *Proc. Natl. Acad. Sci. U.S.A.* **77**, 6458 (1980).
29. G. C. Johnston, J. A. Prendergast, R. A. Singer, *J. Cell Biol.* **113**, 539 (1991).
30. G.-H. Sun, Y. Ohya, Y. Anraku, *Protoplasma* **166**, 110 (1992); S. E. Brockerhoff and T. N. Davis, *J. Cell Biol.* **118**, 619 (1992).
31. Q. Zhu and M. Clarke, *J. Cell Biol.* **118**, 347 (1992).
32. Calmodulin overlays were performed as described by J. R. Glenney and P. Glenney [*Cell* **37**, 743 (1984)], except that the incubations were performed at room temperature with $^{125}$I-labeled calmodulin (NEN) in the presence of 0.1 mM $CaCl_2$.
33. Calmodulin-agarose assays were performed as follows: Fly heads were homogenized at 4°C in a microfuge mortar and pestle (Kontes) in buffer A containing 10 mM imidazole (pH 7.35), 10% sucrose, 5 mM $MgCl_2$, 1 mM dithiothreitol, 160 mM KCl, PMSF (10 μg $ml^{-1}$), and leupeptin (1 μg $ml^{-1}$), and the homogenate was centrifuged at 100,000*g* for 30 min. Calmodulin-agarose (Sigma) was equilibrated in buffer A with several washs and then incubated for 30 min with the head extract supernatant. The extract-bead mixture was centrifuged at 3000*g* for 5 min, and the supernatant was combined with 1× volume of 2× SDS sample buffer and saved for gel analysis. The pellet was washed several times with buffer A plus 340 mM KCl and either 1 mM EGTA or 1 mM $CaCl_2$, and the bound proteins were eluted with SDS sample buffer (volume equal to 2× the supernatant volume). Samples were then fractionated by SDS-PAGE (6% gel).
34. The calmodulin antiserum was raised in rabbits as described by L. J. Van Eldik and D. M. Watterson [*J. Biol. Chem.* **256**, 4205 (1981)]. The antibodies were affinity-purified by their binding to calmodulin-Sepharose and eluted with 3 M sodium thiocyanate. To detect calmodulin from fly retinas, extracts from 25 retinas were prepared and fractionated on an SDS-PAGE (14% gel), transferred to PVDF membrane, and probed with the calmodulin antibody as described by D. Hulen and colleagues [*Cell. Motil. Cytol.* **18**, 113 (1991)], except that $^{125}$I–protein A (NEN) was used instead of a secondary antibody.
35. In less than 10% of the *ninaC*$^{P235}$ samples, which were fixed only with paraformaldehyde, diffuse staining with the antibody to calmodulin was seen over the cell body and rhabdomeres, but when glutaraldehyde and paraformaldehyde were used for fixation, central matrix staining like that in Fig. 4C was seen consistently.
36. We thank D. W. Cleveland and D. J. Montell for helpful comments on this manuscript, J. Lee for technical assistance, and C. B. Klee for antibody to calmodulin. Supported by grant EY08117 from the National Eye Institute (C.M.), the National Science Foundation (Presidential Young Investigator Award to C.M.), and the American Cancer Society (Junior Faculty Research Award to C.M.).

28 May 1993; accepted 8 September 1993

# Crystal Structure of Neocarzinostatin, an Antitumor Protein-Chromophore Complex

Kyoung-Hee Kim, Byoung-Mog Kwon, Andrew G. Myers,* Douglas C. Rees*

**Structures of the protein-chromophore complex and the apoprotein form of neocarzinostatin were determined at 1.8 angstrom resolution. Neocarzinostatin is composed of a labile chromophore with DNA-cleaving activity and a stabilizing protein. The chromophore displays marked nonlinearity of the triple bonds and is bound noncovalently in a pocket formed by the two protein domains. The chromophore π-face interacts with the phenyl ring edges of Phe$^{52}$ and Phe$^{78}$. The amino sugar and carbonate groups of the chromophore are solvent exposed, whereas the epoxide, acetylene groups, and carbon C-12, the site of nucleophilic thiol addition during chromophore activation, are unexposed. The position of the amino group of the chromophore carbohydrate relative to C-12 supports the idea that the amino group plays a role in thiol activation.**

Neocarzinostatin (NCS) is a natural chromoprotein antibiotic isolated from *Streptomyces carzinostaticus* and is composed of a 113–amino acid protein component (apo-NCS) and a labile, nonprotein chromophore component (NCS-chrom) (*1*). A potent cytotoxic agent, NCS has undergone clinical evaluation for antitumor activity (*2*). In the presence of a thiol cofactor, NCS induces cleavage of single- and double-stranded DNA both in vivo and in vitro. The cleavage activity resides exclusively within the chromophore component (*1*), whose structure (*3*) (Fig. 1) was shown previously to include the epoxybicyclo[7.3.0]dodecadienediyne structural element. In vitro, NCS-chrom undergoes efficient thiol addition to form a highly reactive, carbon-centered biradical, which provides a potential molecular basis for the

Division of Chemistry and Chemical Engineering, California Institute of Technology, Pasadena, CA 91125.

*To whom correspondence should be addressed.

antitumor and DNA-cleaving properties of NCS (*4*).

The apoprotein form avidly binds to and greatly stabilizes the labile chromophore; in the absence of apo-NCS, the chromophore degrades rapidly in aqueous solution (*1*). Little is known about the binding of chromophore to protein, although it is frequently conjectured to be noncovalent, and the mechanisms of stabilization and release of the chromophore are equally obscure. The apoproteins of other chromoprotein antibiotics, including actinoxanthin (ACX) and auromomycin [whose apoprotein is macromomycin (MCM)], share extensive (>55%) sequence similarities to NCS (*5–7*), which is reflected in the similarities of the three-dimensional structures of these apoproteins (*8–10*). Computer modeling (*11*) and nuclear magnetic resonance (NMR) studies (*12, 13*) have also been used to derive information on chromophore binding to apo-NCS. The chromophore components of ACX and MCM appear to be distinct from NCS-chrom; available evidence suggests that each apoprotein maintains specificity for its respective chromophore. To establish the chromophore structure and to characterize the protein-chromophore interactions, we determined the three-dimensional structure of both the protein-chromophore complex (holo-NCS) and apo-NCS by x-ray crystallography at 1.8 Å resolution.

The crystal structure analysis of NCS encompassed a combination of multiple isomorphous replacement (MIR), molecular replacement, and noncrystallographic symmetry averaging methods (*14*). The quality of the final $2F_o-F_c$ map calculated at 1.8 Å resolution in the vicinity of the chromophore is illustrated (Fig. 2A). Somewhat surprisingly, although the initial crystallization solution contained a 1:1 complex of NCS protein:chromophore, only one of the NCS protein molecules in the asymmetric unit (designated by residue numbers prefixed with "B") contained the chromophore, while the other NCS protein molecule (designated by residue numbers with the prefix "A") had a 2-methyl-2,4-pentanediol (MPD) molecule in place of the chromophore. The apparent dissociation of chromophore from about half of the NCS molecules in crystals grown from the low pH, aqueous MPD solution is consistent with the known dissociative behavior of NCS in acidic, organic media.

As with the apoprotein structures of ACX, MCM, and NCS (*8–10*), the NCS holoprotein consists primarily of β sheets organized into two domains, with overall dimensions of ~20 Å by 25 Å by 40 Å (Fig. 2B). The larger domain forms a seven-stranded antiparallel β barrel that contains two sheets: an external sheet consisting of strands 1, 2, and 5 (residues 4 to 8, 19 to 24, and 62 to 66, respectively) and an internal sheet formed by strands 4, 3, 6,

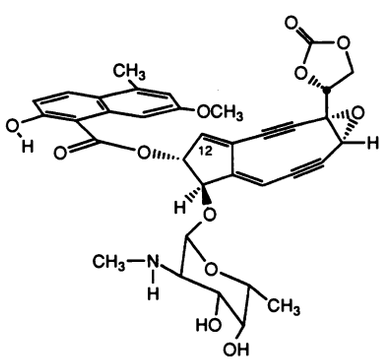


**Fig. 1.** Structure of the NCS chromophore. The position of carbon C-12, the site of thiol addition during activation of the chromophore, is indicated.

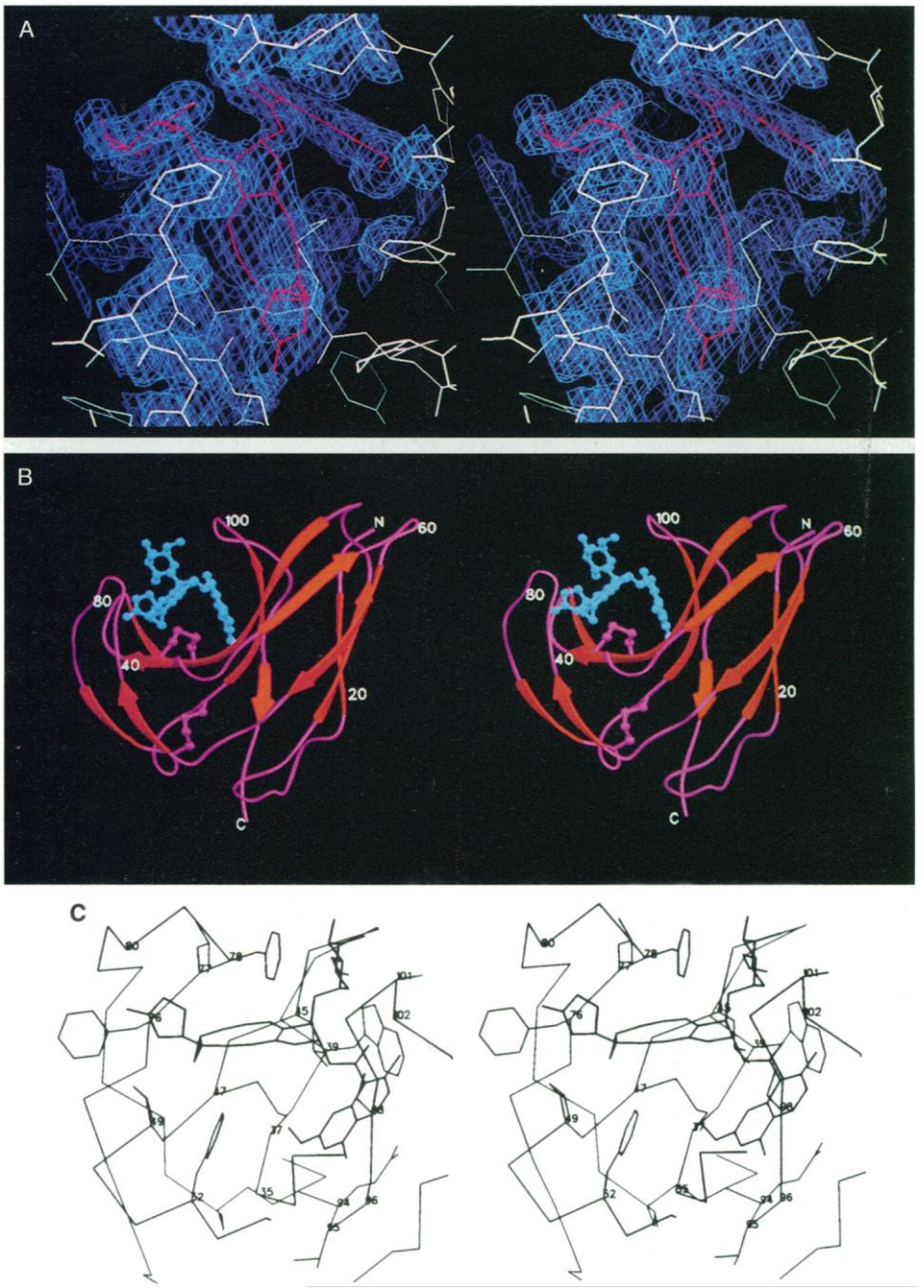


**Fig. 2.** (**A**) Stereoview of the electron density map (blue) of the region surrounding NCS-chrom (red) and neighboring protein (white). The map was calculated with $2|F_o| - |F_c|$ coefficients for data between 5 to 1.8 Å resolution and contoured at 1.0σ. (**B**) Stereoview of the polypeptide fold of holo-NCS. NCS-chrom and cysteine residues are represented by ball-and-stick models. (**C**) Stereoview of the protein environment of NCS-chrom. Residues within 4 Å of the NCS-chrom are labeled. Both (B) and (C) were drawn with the program SETOR (*33*).

and 7 (residues 53 to 57, 30 to 35, 94 to 98, and 108 to 110, respectively). The topology of this NCS domain is similar to that of immunoglobulin (Ig) constant domains (*15*), with the notable exception of the strand 4 "sheet switching" also observed in the topology of the bacterial chaperonin PapD, the D2 domain of CD4, a fibronectin type III domain, and the extracellular domains of human growth hormone receptor (*16*). Despite the topological similarity of the larger domain of NCS with the Ig family, this similarity is not detected by a profile-based sequence analysis (*17*). The smaller domain consists of two twisted, two-stranded, antiparallel β sheets—strands 3a and 3b (residues 36 to 40 and 44 to 48, respectively) and strands 5a and 5b (residues 72 to 75 and 84 to 87, respectively). These two β sheets are almost perpendicular to each other. There is a short segment of $3_{10}$ helix between residues $Pro^{49}$ and $Phe^{52}$; in contrast, there are no helical segments in the structures of MCM or ACX.

The holo-NCS structure is sufficiently well defined to establish that the details of the chromophore structure, including stereochemical assignments, are in complete agreement with the structure (Fig. 1) that was proposed on the basis of synthesis data and $^1H$ NMR spectroscopy (*3*). The epoxy nonadiyne ring of the chromophore is essentially planar, with a root-mean-square (rms) deviation of the nine carbon atoms from the least squares plane of only 0.06 Å. The four C–C≡C bond angles of the two acetylene groups in the enediyne ring, which were not restrained during refinement, display marked nonlinearity with an average value of 161.5° ± 1.2°. The carbohydrate residue of the chromophore adopts a chair conformation, with the amino group oriented above C-12 (the site of nucleophilic thiol addition during activation of the chromophore) at a distance (5 Å) approximating the van der Waals diameter of a sulfur atom. This relation supports the proposal that the amino group plays a role in thiol activation (*18*).

NCS-chrom is bound in the hydrophobic pocket formed by the internal β sheet of the larger domain and the smaller domain (Fig. 2C). The two π-faces of the nine-membered enediyne ring are sandwiched between the $Phe^{B78}$ benzene ring on one side and the $Phe^{B52}$ benzene ring and the disulfide bond $Cys^{B37}$-$Cys^{B47}$ on the other. The $Phe^{B52}$ and $Phe^{B78}$ side chains are perpendicular to the enediyne ring (Fig. 3), which is a favorable orientation often exhibited by aromatic systems (*19*). The positioning of the $Phe^{B78}$ side chain, in particular, should stabilize the chromophore by precluding attack of nucleophiles at C-12. The naphthoate group is at the bottom of the pocket and forms two distorted intramolecular hydrogen bonds to the protein—one between the carbonyl oxygen atom and the Oγ of $Ser^{B98}$, and the other between the methoxyl oxygen atom and the NH of $Gly^{B35}$. There is another hydrogen bond at a lattice contact between the naphthoate hydroxyl oxygen atom and the NH of $Ala^{A1}$, the amino terminus of the other protein molecule in the asymmetric unit. The sugar methylamino group stacks against the $Phe^{B78}$ ring in holo-NCS, which suggests that the amino group in the crystal is protonated. The favorable interaction between a (presumed) positively charged group and the π-face of an aromatic system has been observed in a variety of proteins and model systems (*20*). The enediyne and naphthoate groups of NCS-chrom form van der Waals contacts with many apolar residues ($Gly^{B35}$, $Leu^{B45}$, $Pro^{B49}$, $Leu^{B77}$, $Gly^{B80}$, $Val^{B95}$, $Gly^{B96}$, $Ala^{B101}$, and $Gly^{B102}$) and several aromatic residues ($Trp^{B39}$, $Phe^{B52}$, $Phe^{B76}$, and $Phe^{B78}$) in the binding pocket. The only polar side chains around the chromophore are $Gln^{B94}$ and $Ser^{B98}$. The bound chromophore exposes ~169 $Å^2$ of accessible surface area [as defined by Lee and Richards

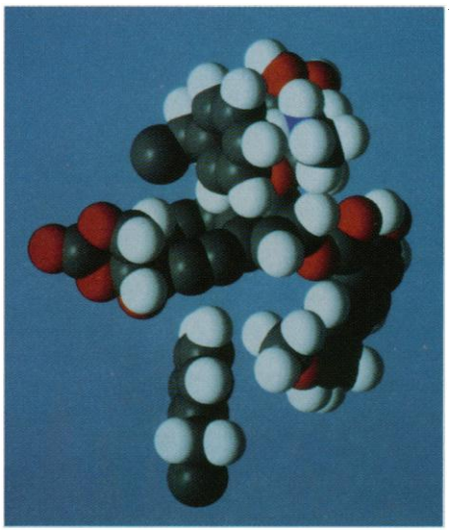

**Fig. 3.** Space-filling model illustrating the packing of NCS-chrom between the side chains of $Phe^{52}$ (bottom) and $Phe^{78}$ (top). The carbonate, amino sugar, naphthoate, and enediyne groups of NCS-chrom are to the left, top, right, and center of the figure, respectively. This figure was prepared with the program MacroModel (*34*), with a coloring scheme of black, white, red, and blue for carbon, hydrogen, oxygen, and nitrogen atoms, respectively.

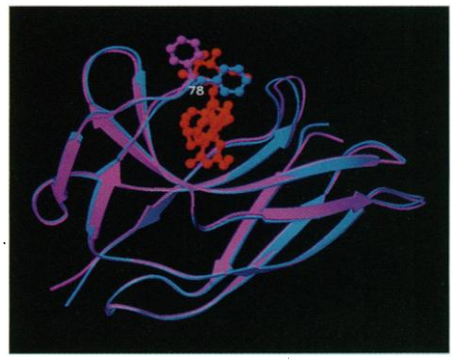


**Fig. 4.** Superposition of apo-NCS and holo-NCS, colored purple and blue, respectively, with the NCS-chrom in red. The positions of the $Phe^{78}$ ring in the two forms of the NCS structure are represented by ball-and-stick models.

**Table 1.** Data collection and phasing statistics. The native I data set was used for calculation of MIR phases, averaging, and solvent flattening and in the first stage of model building and refinement. The native II data set was 94.6% complete to 1.8 Å resolution and was used for the final refinement. The samarium and iridium compounds were only used for phasing to 5.0 Å resolution.

| Parameter | Native I | Native II | $(CH_3)_3Pb(OAc)$ | $(CH_3)_3PbCl$ | $Sm(OAc)_3$ | $K_3IrCl_6$ |
|---|---|---|---|---|---|---|
| Collected reflections (no.) | 31,730 | 146,707 | 20,021 | 18,553 | 24,770 | 19,985 |
| Unique reflections (no.) | 9,024 | 23,556 | 5,883 | 5,678 | 5,865 | 6,280 |
| Resolution (Å) | 2.40 | 1.70 | 2.77 | 2.79 | 2.78 | 2.68 |
| Completeness (%) | 92.7 | 87.8 | 94.6 | 91.1 | 94.3 | 91.5 |
| $R_{merge}$* | 0.071 | 0.077 | 0.072 | 0.104 | 0.091 | 0.047 |
| $R_{iso}$† (50.0 to 3.0 Å) | | | 11.9 | 11.1 | 12.6 | 13.0 |
| Soaking concentration (mM) | | | 10 | 14 | 10 | Saturated |
| Soaking time (hours) | | | 24 | 48 | 24 | 24 |
| Binding sites (no.) | | | 1 | 1 | 1 | 1 |
| Binding locations | | | $Asp^{A33}$ | $Asp^{A33}$ | $Glu^{A106}$ $Glu^{B106}$ | $Arg^{B71}$ |
| Phasing power‡ (10.0 to 3.0 Å) | | | 1.54 | 1.30 | 0.46 | 0.75 |

*$R_{merge} = \Sigma_h\Sigma_i|I(h)_i - \langle I(h)\rangle|/\Sigma_h\Sigma_i I(h)_i$, where $I(h)$ is the intensity of reflection $h$, $\Sigma_h$ is the sum over all reflections, and $\Sigma_i$ is the sum over the $i$ measurements of reflection $h$. †$R_{iso} = \Sigma_h|F_{PH} - F_P|/\Sigma_h F_P$, where $F_P$ and $F_{PH}$ are the native and derivative structure factor amplitudes, respectively. ‡Phasing power = $F_H(calc)/E$, where $F_H$ is the average heavy atom structure amplitude, and $E$ is the estimated lack of closure error.

(*21*)] to the solvent, or about 18% of the total accessible area of the free NCS-chrom. The solvent-exposed regions of NCS-chrom are provided primarily by the amino sugar, carbonate, and naphthoate hydroxyl groups.

The crystallographically observed binding interactions between the chromophore and NCS protein differ in several important respects from models proposed on the basis of computer modeling (*11*) and NMR studies (*12, 13*). These differences are most notably reflected in the orientation of NCS-chrom in the binding pocket between the two domains of the NCS protein. In the computer model, the NCS-chrom appears rotated by ~180° relative to the crystallographically determined orientation, thus exchanging the naphthoate and enediyne ring positions. Although the NCS-chrom orientation in the NMR structures more closely resembles the crystallographic structure, many features of the protein-chromophore binding, such as the π interactions between the side chains of $Phe^{52}$ and $Phe^{78}$ and the chromophore enediyne and amino sugar groups, were not observed.

The structures of apo-NCS and holo-NCS are similar, with rms deviations of 0.59 Å for 113 Cα atoms and 0.31 Å for 35 Cα atoms in the seven-stranded β barrel of the larger domain. Only $Gly^{84}$, $Thr^{85}$, $Ala^{101}$, and the two terminal residues have differences greater than 1.0 Å in Cα positions between holo- and apo-NCS. The most noteworthy change between holo-NCS and apo-NCS is the position of the $Phe^{78}$ ring (Fig. 4). This side chain rotates from a position over the enediyne ring in holo-NCS to a solvent-exposed position in apo-NCS, where it abuts the side chain of $Asp^{A79}$. This amino acid interaction may underlie the pH-sensitive dissociation of chromophore from NCS. Differences between apo-NCS and holo-NCS in strands 5a and 5b, and in the loops between strands 5a and 5b, 3a and 3b, and 6 and 7, increase the width of the binding pocket to about 10 Å so as to accommodate the chromophore. In the absence of NCS-chrom, a hydrogen bond in the crystal between MPD and the Oγ of $Ser^{A98}$ of apo-NCS replaces the distorted hydrogen bond between the chromophore and Oγ of $Ser^{B98}$ in holo-NCS.

The NCS, MCM, and ACX proteins share the same basic structural architecture. The common core of these proteins (*22*) contains 90 residues (80% of the total). The rms deviations for the common core are 0.76 Å between holo-NCS and MCM, 1.27 Å between holo-NCS and ACX, and 1.17 Å between MCM and ACX. The regions outside the common core (residues 26 to 30, 41 to 44, 78 to 79, and 99 to 107) are less conserved and, except for $Phe^{78}$ and $Asp^{79}$, correspond to the complementarity-determining regions in the Ig variable domains. The most conserved sequence region in the structure is strand 3a, which connects the larger and smaller domains. The binding pockets of NCS, ACX, and MCM have similar overall shapes, but the locations of side chains around the binding pockets are quite different. Among 18 residues close to NCS-chrom, only four—$Cys^{37}$, $Cys^{47}$, $Gly^{80}$, and $Gly^{96}$—are conserved. The binding selectivity between a protein and its respective chromophore must therefore be the result of interactions between the chromophore and specific side chains, such as $Phe^{78}$ of NCS, that represent variable elements within the protein structures.

## REFERENCES AND NOTES


1. N. Ishida, K. Miyazaki, K. Kumagi, M. Rikimaru, *J. Antibiot. Ser. A* **18**, 68 (1965); J. Shoji, *ibid.* **14**, 27 (1961); M. A. Napier, B. Holmquist, D. J. Strydom, I. H. Goldberg, *Biochem. Biophys. Res. Commun.* **89**, 635 (1979); Y. Koide *et al.*, *J. Antibiot.* **33**, 342 (1980); L. S. Kappen, M. A. Napier, I. H. Goldberg, *Proc. Natl. Acad. Sci. U.S.A.* **77**, 1970 (1980).
2. H. Maeda, *Anticancer Res.* **1**, 175 (1981); D. D. Von Hoff, D. A. Amato, J. H. Kaufman, G. Falkson, T. J. Cunningham, *Am. J. Clin. Oncol.* **7**, 135 (1984); G. Falkson *et al.*, *J. Clin. Oncol.* **2**, 581 (1984); A. Kimoto, T. Konno, T. Kawaguchi, Y. Miyauchi, H. Maeda, *Cancer Res.* **52**, 1013 (1992); T. Konno, *Eur. J. Cancer* **28**, 403 (1992), and references therein.
3. K. Edo *et al.*, *Tetrahedron Lett.* **26**, 331 (1985); K. Edo *et al.*, *J. Antibiot.* **39**, 1615 (1986); A. G. Myers, P. J. Proteau, T. M. Handel, *J. Am. Chem. Soc.* **110**, 7212 (1988).
4. A. G. Myers, *Tetrahedron Lett.* **28**, 4493 (1987); ——— and P. J. Proteau, *J. Am. Chem. Soc.* **111**, 1146 (1989).
5. H. Maeda, C. B. Glaster, J. Czombos, J. Meienhofer, *Arch. Biochem. Biophys.* **164**, 379 (1974); B. W. Gibson, W. C. Herlihg, T. S. Anantha Samy, *J. Biol. Chem.* **259**, 10801 (1984); K. Kuromizu, S. Tsunasawa, H. Maeda, O. Abe, *Arch. Biochem. Biophys,* **246**, 199 (1986); N. Sakata *et al.*, *Biol. Pharm. Bull.* **16**, 26 (1993).
6. A. S. Khokholov *et al.*, *J. Antibiot.* **22**, 541 (1969).
7. H. Chimura *et al.*, *ibid.* **21**, 44 (1968).
8. V. Z. Pletnev, A. P. Kuzin, S. D. Trakhanov, P. V. Kostetsky, *Biopolymers* **21**, 287 (1982).
9. P. Van Roey and T. A. Beerman, *Proc. Natl. Acad. Sci. U.S.A.* **86**, 6587 (1989).
10. X. Gao, *J. Mol. Biol.* **225**, 125 (1992); E. Adjadj, E. Quiniou, J. Mispelter, V. Favaudon, J.-M. Lhoste, *Eur. J. Biochem.* **203**, 505 (1992); M. Lyndsay Remerowski, S. J. Glaser, L. C. Sieker, T. S. Anantha Samy, G. P. Drobny, *Biochemistry* **29**, 8401 (1990); A. Teplyakov, G. Obmolova, K. Wilson, K. Kuromizu, *Eur. J. Biochem.* **213**, 737 (1993).
11. M. Ishiguro, S. Imajo, M. Hirama, *J. Med. Chem.* **34**, 2366 (1991).
12. T. Tanaka *et al.*, *Tetrahedron Lett.* **32**, 3175 (1991).
13. T. Tanaka, M. Hirama, K. Fujita, S. Imajo, M. Hirama, *Chem. Commun.* **15**, 1205 (1993).
14. Structure analysis: Crystals of NCS were grown at 4°C by the vapor diffusion method. The hanging drops contained equal volumes of a 20 mg/ml solution of NCS [dissolved in 50 mM sodium acetate buffer (pH 5.0)] and the reservoir solution [70% MPD, 50 mM sodium acetate buffer (pH 4.6)]. Rod-shaped crystals grow in space group $P6_5$ with cell dimensions $a = b = 90.4$ Å and $c = 52.5$ Å and two protein molecules per asymmetric unit. This crystal form is distinct from that previously reported by Sieker (*23*). We prepared four derivatives by soaking crystals in solutions containing a heavy-atom compound (Table 1). Because the crystals were very sensitive to x-ray radiation, all data were collected at ~−160°C as in (*24*). Native data set I and derivative data sets (Table 1) were collected with a Siemens multiwire area detector mounted on a Siemens rotating anode generator and were processed with the program packages XENGEN (*25*) and ROCKS (*26*). Native data set II (Table 1) was collected on the R-AXIS imaging plate system mounted on a Rigaku rotating anode generator and processed with the R-AXIS software. Binding sites for the heavy atoms were determined from difference Patterson maps, with the correct relative origin established from difference Fourier maps. Heavy atom parameters were refined with the program PHARE, yielding MIR phases with a figure of merit of 0.58 (10.0 to 3.0 Å, 4779 reflections). The general noncrystallographic symmetry relation between two molecules in the asymmetric unit was determined by density correlation studies (*27*) and manual molecular replacement (*28*) with the MCM structure (*9*) as a model. Iterative averaging and solvent flattening (*29*) were used to improve the MIR and molecular replacement phases. Two protein molecules were built with the graphics program TOM/FRODO (*30*). For coordinate refinement, we used the program TNT (*31*) during the initial stages of modeling and X-PLOR (*32*) for the final stages. The final model contains two protein molecules, one chromophore, one MPD, and 161 water molecules (1773 atoms total) in the asymmetric unit. This model has an *R* factor of 19.9% between 5.0 and 1.8 Å resolution with rms deviations from ideal bond distances and angles of 0.014 Å and 2.84°, respectively. $Pro^9$ adopts the *cis* peptide conformation and is conserved in the structures of MCM (*9*) and ACX (*8*). The Ramachandran plot shows no residues in unfavorable regions. Refined coordinates have been deposited in the Brookhaven Protein Data Bank (entry code 1NCO).
15. J. Deisenhofer, *Biochemistry* **20**, 2361 (1981).
16. A. Holmgren and C. I. Branden, *Nature* **342**, 248 (1989); S.-E. Ryu *et al.*, *ibid.* **348**, 419 (1990); D. J. Leahy, W. A. Hendrickson, I. Aukhil, H. P. Erickson, *Science* **258**, 987 (1992); A. M. deVos, M. Ultsch, A. A. Kossiakoff, *ibid.* **255**, 306 (1992).
17. P. Bork and R. F. Doolittle, *Proc. Natl. Acad. Sci. U.S.A.* **89**, 8990 (1992).
18. A. G. Myers, P. M. Harrington, B.-W. Kwon, *J. Am. Chem. Soc.* **114**, 1086 (1992).
19. S. K. Burley and G. A. Petsko, *Science* **229**, 23 (1985).
20. D. A. Dougherty and D. A. Stauffer, *ibid.* **250**, 1558 (1990); J. L. Sussman *et al.*, *ibid.* **253**, 872 (1991); D. A. Rodham *et al.*, *Nature* **362**, 735 (1993); M. Levitt and M. F. Perutz, *J. Mol. Biol.* **201**, 751 (1988).
21. B. Lee and F. M. Richards, *J. Mol. Biol.* **55**, 379 (1971).
22. C. Chothia and A. M. Lesk, *EMBO J.* **5**, 823 (1985).
23. L. C. Sieker, L. H. Jensen, T. S. Anantha Samy, *Biochem. Biophys. Res. Commun.* **68**, 358 (1976).
24. H. Hope, *Acta Crystallogr. B* **44**, 22 (1988).
25. A. J. Howard *et al.*, *J. Appl. Crystallogr.* **20**, 383 (1987).
26. G. N. Reeke, *ibid.* **17**, 125 (1984); P. Bethge, *ibid.*, p. 215.
27. J. M. Cox, *J. Mol. Biol.* **28**, 151 (1967).
28. A large peak at (0, 0, 0.5) in the native Patterson map calculated at low (~8 Å) resolution indicated that a noncrystallographic twofold axis was roughly parallel to the crystallographic *c* axis. The twofold axis was refined with a density correlation algorithm (*27*) and was then used to refine the phases by noncrystallographic symmetry averaging (*29*). The MCM structure (*9*) was manually fit to a 5 Å resolution electron density with the graphics program TOM (*30*), followed by rigid body refinement by TNT (*31*). The final relation between the two molecules is described by the Euler angles $\theta_1 = 165.15°$, $\theta_2 = 10.20°$, and $\theta_3 =$

22.37° and a translation of 91.61 Å, −3.69 Å, and −1.75 Å, respectively, in an orthogonal coordinate system.
29. G. Bricogne, *Acta Crystallogr.* **32**, 832 (1976); M. G. Rossmann, Ed., *The Molecular Replacement Method* (Gordon and Breach, New York, 1972).
30. T. A. Jones, *Methods Enzymol.* **115**, 157 (1985).
31. D. E. Tronrud, L. F. Ten Eyck, B. W. Matthews, *Acta Crystallogr. A* **43**, 489 (1987).
32. A. T. Brünger, *J. Mol. Biol.* **203**, 803 (1988).
33. S. V. Evans, *J. Mol. Graphics*, in press.
34. W. C. Still *et al.*, MacroModel V2.5, Department of Chemistry, Columbia University, New York (1988).
35. We thank L. Joshua-Tor and B. T. Hsu for their many contributions to this project, P. J. Bjorkman for discussions, and P.-van Roey for providing the refined MCM coordinates. NCS powder was a generous gift of Kayaku Co., Ltd. Supported by NIH (CA47148) (A.G.M.), with partial support of the x-ray facility (GM45162) (D.C.R.) and instrumentation provided by the Beckman Institute and the Irvine Equipment fund.

24 June 1993; accepted 13 September 1993

# An Archimedian Spiral: The Basal Disk of the *Wolinella* Flagellar Motor

Harald Engelhardt, Stephan C. Schuster,* Edmund Baeuerlein†

**The motor that powers the rotation of the bacterial flagellum reaches through both membranes into the cytoplasm of Gram-negative bacteria. The flagellum is connected by a flexible link (hook) to the motor axis, which passes through the center of a structure called the basal disk. The basal disk functions with the L-P ring complex as a bushing, enabling the rotation of the motor in the cell wall. The protein subunits of the basal disk of *Wolinella succinogenes* form an Archimedian spiral. The polymerization of subunits from a nucleation point at the motor in the form of a spiral allows constant growth of the basal disk. The disk is thought to provide a reinforcement at the flagellar insertion at the cell pole and to disperse forces that are generated by the momentum of the flagellar rotation.**

Flagellar motors (*1–3*) of many bacteria are inserted exclusively at cell poles rather than distributed over the cell body. These motors display a structural element called a basal disk. Basal disks (*4, 5*) are attached to the inner side of the outer membrane and contain the L-P ring complex (*3*), a bushing of the flagellar motor. Both elements form part of the stator, anchoring the motor axis and other rotating parts of the motor to the cell wall (Fig. 1) (*6*).

Earlier reports described basal disk structures associated with the flagellar apparatus in various species of proteobacteria (*7–11*) and more recently one (*12*) in members of the *Comamonadaceae* and disk-like septa occurring between cells of some archaebacteria (*13*). It was assumed that these basal disks were an assembly of concentric rings (*5, 7, 8*). We used electron microscopy to investigate basal disks from *W. succinogenes* (*5, 14*), a Gram-negative uniflagellated bacterium that features a disk of an average diameter of 170 nm. Disks were isolated either with basal bodies or, after disruption of the motor axis, as basal disks with an integrated L-P ring complex in their center (Fig. 2) (*15*). Basal disks from a stationary grown culture display roughly the same diameter, whereas disks isolated from early logarithmic cultures show a large deviation from the average 170-nm diameter toward smaller diameters (Fig. 3) (*16*). This suggests that the disks are assembled by the addition of subunits in a way that does not disturb the preexisting structure. Subunits of the basal disks are assembled in a radial geometry around the central ring structure (L-P ring), as seen by visual inspection. This suggests two possible geometric forms for the underlying construction: a set of concentric rings or a spiral.

We describe here a procedure that allowed us to distinguish concentric rings from spirals by the analysis of their Fourier transforms (*17, 18*). This differentiation is not possible by investigating the optical diffractograms of electron micrographs alone. In the Fourier transforms, concentric rings possess information exclusively in the real part, representing the symmetric structural information. Spirals, however, show symmetric and asymmetric contributions, with the odd-numbered diffraction orders occurring in the imaginary part and the even-numbered diffraction orders in the real part of the Fourier transform. For the disks of *W. succinogenes*, the significant first-order ring is in the imaginary part (Fig. 4D) and consists of fringes that are arcs of a spiral. This proves that the basal disk is a spiral (Fig. 4B). The spiral line can be observed clearly in the filtered image of a small disk (Fig. 4B), and the end of the spiral band is even visible in the original micrograph (Fig. 4A).

H. Engelhardt, Department for Structural Biology, Max Planck Institute for Biochemistry, D-82152 Martinsried, Germany.
S. C. Schuster and E. Baeuerlein, Department for Membrane Biochemistry, Max Planck Institute for Biochemistry, D-82152 Martinsried, Germany.
*Present address: Biology Division 147-75, California Institute of Technology, Pasadena, CA 91125.
†To whom correspondence should be addressed.

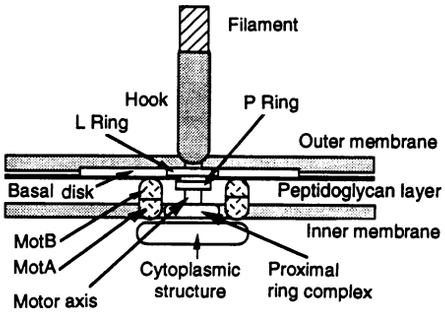


**Fig. 1.** Schematic illustration of the bacterial flagellar motor of *W. succinogenes*. The flagellar motor is composed of a filament, hook, motor axis, basal disk, L ring, P ring, proximal ring complex, cytoplasmic structure, and the MotA and MotB proteins. The motor penetrates the outer membrane, the peptidoglycan layer, and the inner membrane.

The individual subunits along one whorl of the spiral also contribute to the Fourier transform. Their Fourier coefficients are included in the real part as well as in the imaginary part of the transform. Model calculations have shown that their contributions are less prominent than the spiral information. The corresponding diffraction "rings" formed by radially and spatially distributed diffraction spots are weak (Fig. 4C). The filtered image (Fig. 4B) suggests that the spatial distance between the molecules along the spiral line is about equal to the radial distance between neighboring parts of the spiral. Thus, the spatial contributions of subunits along one whorl and between whorls overlap in the Fourier transform (Fig. 4C). The disk has the features of an Archimedian spiral, which is described in polar coordinates by

$$r = \frac{d\varphi}{2\pi}$$

**Fig. 2.** Basal disks of the flagellar motor from the Gram-negative bacterium *W. succinogenes*. The disk on the left has the hook–basal body complex in place, whereas the disk on the right lost the complex by a short ultrasonic treatment. Disintegration of the motor axis was necessary to obtain free basal disks. The central hole is visible with a diameter of 11 nm, which is close to the diameter of the motor axis. The central ring of the basal disk is part of the L-P ring complex, a bearing of the motor.